Effects of grid geometry on non-equilibrium dissipation in grid turbulence

Koji Nagata, Teppei Saiki, Yasuhiko Sakai, Yasumasa Ito, and Koji Iwano

Citation: Physics of Fluids **29**, 015102 (2017); doi: 10.1063/1.4973416
View online: http://dx.doi.org/10.1063/1.4973416
View Table of Contents: http://aip.scitation.org/toc/phf/29/1
Published by the American Institute of Physics

PHYSICS OF FLUIDS **29**, 015102 (2017)

Effects of grid geometry on non-equilibrium dissipation in grid turbulence

Koji Nagata,[1,a)] Teppei Saiki,[2] Yasuhiko Sakai,[2] Yasumasa Ito,[2] and Koji Iwano[2]
[1]*Department of Aerospace Engineering, Nagoya University, Nagoya 464-8603, Japan*
[2]*Department of Mechanical Science and Engineering, Nagoya University, Nagoya 464-8603, Japan*

(Received 24 April 2016; accepted 13 December 2016; published online 4 January 2017)

A total of 11 grids in four families, including single- and multi-scale grids, are tested to investigate the development and decay characteristics of grid-generated turbulence. Special attention has been focused on dissipation and non-equilibrium characteristics in the decay region. A wide non-equilibrium region is observed for fractal square grids with three and four iterations. The distributions of the Taylor microscale λ, integral length scale L_u, and dissipation coefficient C_ε show that a simple combination of large and small grids does not reproduce elongated non-equilibrium regions as realized by the fractal square grid. On the other hand, a new kind of grid, quasi-fractal grids, in which the region of the smaller fractal elements ($N = 2$–4) of the fractal square grid is replaced by regular grids, successfully reproduce a similar flow field and non-equilibrium nature to that seen in the fractal square grid case. This suggests that the combination of large square grid and inhomogeneously arranged smaller grids produces an elongated non-equilibrium region. The dissipation coefficient C_ε is better collapsed using $Re_0 = t_0 U_\infty/\nu$ (where t_0 is the thickness of the largest grid bar, U_∞ the inflow velocity, and ν the kinematic viscosity) as a global/inlet Reynolds number rather than $Re_M = MU_\infty/\nu$ (where M is the mesh size) [P. C. Valente and J. C. Vassilicos, "Universal dissipation scaling for non-equilibrium turbulence," Phys. Rev. Lett. **108**, 214503 (2012)]. *Published by AIP Publishing.* [http://dx.doi.org/10.1063/1.4973416]

I. INTRODUCTION

Since the first experiments performed by Hurst and Vassilicos,[1] turbulence generated by multi-scale grids has been investigated both experimentally[2–17] and numerically.[17–24] The practical applications of fractal grids (FGs) or plates have also been explored, including a flow meter using a fractal orifice,[25,26] reduction of spoiler noise,[27] turbulence generators for combustion,[28,29] etc.

The most interesting and important finding may be the existence of a non-equilibrium region in the initial stage of turbulence kinetic energy (TKE) decay.[4] Seoud and Vassilicos[2] first showed that the "cornerstone dissipation scaling of turbulence theory,"[30] in which

$$C_\varepsilon = \frac{\varepsilon}{u'^3/L_u} = \frac{L_u/\lambda}{Re_\lambda} \tag{1}$$

is constant, does not hold for fractal-generated turbulence. Here, C_ε is the dissipation coefficient, ε the TKE dissipation rate, u' the streamwise rms velocity, L_u the integral length scale, λ the Taylor microscale, and $Re_\lambda = \lambda u'/\nu$ (where ν is the kinematic viscosity) the local turbulent Reynolds number. This implies that the Richardson-Kolmogorov equilibrium cascade does not hold.[3,4,13,30] Extensive review of this subject has been done by Vassilicos.[30] Note that the non-constant value of C_ε at low Reynolds numbers (typically $Re_\lambda < 50$–100)[30–34] is due to the viscous effect. Our interest here is in the non-constant value of C_ε encountered at sufficiently large Reynolds numbers. Note also that, in some flows, large and small scales are coupled strongly, or the so-called inverse cascade is even observed, which contradicts the Richardson-Kolmogorov cascade concept (see, for example, Tsinober[35] and references therein). By defining turbulence as "an eddy-like state of fluid motion where the inertial-vortex forces of the eddies are larger than any other forces" (i.e., a narrow definition of turbulence), Gibson[36,37] has argued that turbulence always starts at small scales and cascades to large scales, and this cascade mechanism has been explained by the internal vortex pairing. However, our interest in this paper is limited to equilibrium/non-equilibrium dissipation in grid turbulence (turbulence here being defined conventionally or broadly), and investigating inverse cascades is beyond the scope of this paper.

Valente and Vassilicos[6] (see also Vassilicos[30]) further showed that in the near field of grid turbulence

$$C_\varepsilon \propto \frac{Re_M}{Re_L} \propto \frac{Re_M^{1/2}}{Re_\lambda}. \tag{2}$$

Here, $Re_M = MU_\infty/\nu$ (where M is the mesh size and U_∞ is the inflow velocity) is the mesh (or global/inlet) Reynolds number, $Re_L = L_u u'/\nu$ the local turbulent Reynolds number based on L_u. This non-equilibrium nature of turbulence has also been confirmed in subsequent experiments, for both regular and multi-scale grids.[13–15,38] A scale-by-scale energy budget has also been measured in multi-scale[12,16] and regular[39] grid turbulence. Hearst and Lavoie[12] proposed that non-zero transverse transport of TKE and the production due to transverse mean velocity gradients cause an imbalance of the scale-by-scale energy budget in the near field. Valente and Vassilicos[39]

[a)] Author to whom correspondence should be addressed. Electronic mail: nagata@nagoya-u.jp.

TABLE I. Geometry of the grids.

Grid	FG1	FG2	FG3	FG4	RG2	RG3	RG4	CRG12	CRG15	QFG8	QFG18
L_0 or M (mm)	163.8				163.8	78.8	78.8	163.8		163.8	
t_0 (mm)	11.7				20.1	13.4	10.1	11.7	14.5	11.7	
L_r	···	2.08	4.30	8.95	···			4.30	5.64	8.59	20.7
t_r	···	2.39	5.57	13.0	···			5.57	13.0	5.37	13.0
σ (%)	8.5	15.0	20.0	25.0	25.0			25.0		25.0	
X_* (mm)	2293				1335	463	618	2293	1850	2293	
M_{eff} (mm)	124.2	65.5	34.1	18.2	95.1	72.2	58.2	26.9	22.8	19.6	9.3

also found an imbalance between the energy transfer to small scales and the dissipation in the non-equilibrium region and showed that this imbalance is reflected on the small-scale advection. They also demonstrated that the production and transport of turbulence are large-scale phenomena that do not affect the energy transfer to small scales. On the other hand, Hearst and Lavoie[15] suggested from the measurement of velocity derivative skewness that the residual strain from turbulence-generating conditions is likely to lead to non-equilibrium properties.

Despite extensive previous studies, the role of the fractal elements of the fractal grid and what kind of geometry (or grid arrangement) causes the elongated non-equilibrium region for the fractal grids are less understood. In this study, we design and manufacture two types of new grids, which are basically the combinations of large and small grids, and investigate the flow field and TKE dissipation. Finally, we show that the combinations of large square grid and inhomogeneously arranged smaller grids produce elongated non-equilibrium regions along the centerline.

II. EXPERIMENTS

A. Wind tunnel

The wind tunnel used was the same as that used in our previous study.[10] The cross-sectional area of the test section was $T^2 = 300 \times 300$ mm^2 with a length of 3800 mm. Centerline statistics downstream of the fractal square grid[10] were in good agreement with previous studies[1,3] that used similar grid and were performed at the same Reynolds number based on U_∞ and the thickness of the largest grid bar t_0, $Re_0 = t_0 U_\infty/\nu$. For details about the wind tunnel, see our previous paper.[10]

B. Grids

A total of 11 grids in four families were tested: fractal grids (FGs) with an iteration of $N = 1$–4, regular grids (RGs), combined regular grids (CRGs), and quasi-fractal grids (QFGs).

The fractal grid with $N = 4$ (Fig. 1(d)) was identical to that used in our previous study.[10] Its geometry is tabulated in Table I. Here, L_0 is the length of the largest grid bar (for regular grids, this corresponds to the mesh size M); L_r (t_r) the length (thickness) ratio between the largest and smallest grid bars; σ the blockage ratio; and M_{eff} the effective mesh size[1] defined as $M_{eff} = \frac{4T^2}{P}\sqrt{1-\sigma}$, where P is the perimeter of the grid. The streamwise thickness was 5 mm for all the grid elements. More details of this grid can be found in our previous study.[10] FG1 consisted only of the largest grid element of FG4. Likewise, FG2 consisted of the largest and the second-largest grid elements of FG4, and FG3 was obtained by removing the smallest grid elements from FG4. Naturally, σ differed for each grid. FG1 was made of stainless steel. FG2 and FG3 were made from polymethyl methacrylate (PMMA) and were produced using a laser cutter. They were suspended by a thin (0.1-mm-diameter) piano wire. We confirmed by measuring the wake behind the wire that the effects of the wire on the velocity fields were negligible. FG4 was made from epoxy resin and fabricated by rapid prototyping.

The regular grids (RG2, RG3, and RG4: Fig. 2), made of iron, consisted of square bars and had uniform square meshes. RG2 and RG3 were monoplane and RG4 was biplane in construction. The mesh size of RG2 was equivalent to L_0 for FG1–FG4 and those of RG3 and RG4 were equivalent to that of the second iteration of FG2–FG4. Note that the center of RG3 was obstructed while that of RG4 was unobstructed. All regular grids had the same σ as FG4.

The combined regular grids (CRG12 and CRG15: Fig. 3) consisted of two "regular" grids with different mesh sizes. The mesh size of the larger "regular" grid was equivalent to L_0 for FG1–FG4 (and also to the mesh size of RG2). The mesh size of the smaller "regular" grid of CRG12 was equivalent to the third iteration (L_2) for FG4 (and therefore, to the smallest element of FG3). Thus, L_r for CRG12 was equivalent to that of FG3. The mesh size of the smaller "regular" grid of CRG15 lay between the third (L_2) and fourth (L_3) elements of FG4. The thickness ratio t_r of CRG12 was equivalent to that of FG3, and that of CRG15 was equivalent to that of FG4.

Replacing the region of smaller fractal elements ($N = 2$–4) of FG4 by regular grids, we obtained the quasi-fractal grids QFG8 and QFG18 (Fig. 4). The difference between CRGs and QFGs is that, in CRGs, a smaller "regular" grid covers the entire region while, in QFGs, only the regions of smaller fractal elements are replaced by the "regular" grid. L_0 and t_0 were the same as those for FG4 (and CRG12). These grids were designed to investigate whether or not the presence of fractals is important in creating the specific nature of fractal grid turbulence.[2,4] We call the region replaced by the smaller "regular" grid the "shielding area," and other (cross-shaped) regions the "open area." The mesh size of the smaller "regular" grid of QFG8 was close to that of the smallest grid element

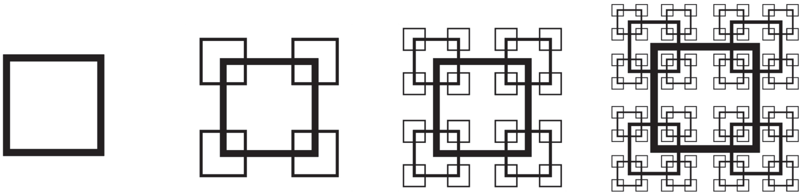
(a) FG1 (b) FG2 (c) FG3 (d) FG4

FIG. 1. Fractal grids (FGs).

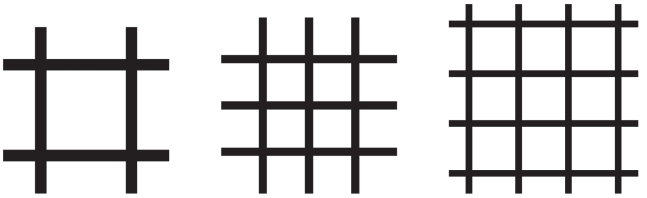
(a) RG2 (b) RG3 (c) RG4

FIG. 2. Regular grids (RGs).

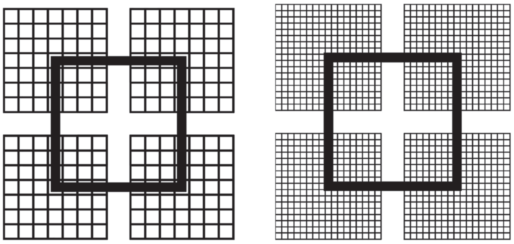
(a) QFG8 (b) QFG18

FIG. 4. Quasi fractal grids (QFGs).

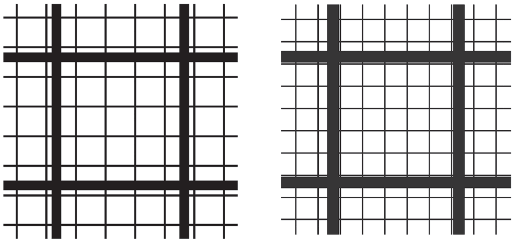
(a) CRG12 (b) CRG15

FIG. 3. Combined regular grids (CRGs).

(L_3) of FG4, and the thickness of the smaller "regular" grid of QFG18 was equivalent to that of the smallest grid element (t_3) of FG4. Thus, L_r for QFG8 was close to that of FG4, and t_r for QFG18 was equivalent to that of FG4 (and CRG15).

For CRGs and QFGs, the grids were monoplanar and their streamwise thickness was 5 mm. The grids were made from VeroWhite using a 3D printer. Both grids had the same σ as FG4 (and RGs).

C. Measurement system and flow conditions

A constant-temperature anemometer (DANTEC StreamLine) with an I-type hot-wire probe (DANTEC 55P11) was used to measure instantaneous streamwise velocity. The diameter of the wire was 5 μm and its length was 1.25 mm. The probe was calibrated in the wind tunnel, and the instantaneous streamwise velocity was calculated according to King's law. The sampling rate was set to 50 kHz to obtain reliable derivative quantities, e.g., TKE dissipation rate ε. A low-pass filter was used to remove noise.[34] The cutoff frequency was determined by the measured frequency spectra at each location. The data sampling number was 5 242 880 ($=5 \times 2^{20}$) and 13 measurements were conducted at each location to reduce statistical uncertainties.

The experiments were conducted at Re_0 = 5900 and 11 400, the same as in previous studies[1,3,10] except for the RG4 grid: Re_0 = 11 400 was not attainable because of the high required wind speed U_∞. For RG2, measurements at Re_M = 82 600 and 159 600 (corresponding to Re_0 = 5900 and 11 400 for FG4) were added. For RG3 and RG4, measurements at Re_M = 82 600 (corresponding to Re_0 = 5900 for FG4) were added. The values of Re_0 and Re_M are listed in Table II.

In most figures, the streamwise distance from the grid X is normalized by the wake interaction length scale, $X_* = L_0^2/t_0$, which was first introduced by Mazellier and Vassilicos[3] and used in subsequent studies on both fractal and regular grids. Figures for the regular grids (i.e., RG2, RG3, and RG4) are

TABLE II. Reynolds numbers.

Grid	FG1 FG2 FG3 FG4	RG2	RG3	RG4	CRG12	CRG15	QFG8 QFG18
Re_0	5 900	5 900	5 900	5 900	5 900	5 900	5 900
	11 400	11 400	11 400	···	11 400	11 400	11 400
Re_M	82 600	48 100	34 700	46 000	82 600	66 600	82 600
	159 600	92 900	67 000	···	159 600	128 800	159 600
		82 600	82 600	82 600			
		(Re_0 = 10 100)	(Re_0 = 14 000)	(Re_0 = 10 600)			
		159 600					
		(Re_0 = 19 600)					

also plotted against X/M or X/L_0 following the conventional manner.

III. RESULTS AND DISCUSSION

In Sections III A–III D, centerline statistics at $Re_0 = 5900$ are shown because the RG4 grid cannot be tested at $Re_0 = 11\,400$. Note that we did not find any significant qualitative difference between $Re_0 = 5900$ and 11 400.

A. Rms velocity

Figure 5 shows the centerline rms velocity u'_c normalized by U_∞. For FGs (Fig. 5(a)), u'_c increases as N increases. This is largely due to the increase in σ. However, it can be seen that a rapid increase of u'_c near the grid is already established for FG3. On the other hand, comparing FG3 and FG4, large u'_c in the downstream region is caused by the existence of the smallest grid element of FG4. Note that we also take into account the increase in σ from FG3 to FG4. Looking at the streamwise location X_{peak} where u'_c exhibits its peak value, X_{peak} for FG4 is closer to the origin than that for FG1. The result agrees qualitatively with our previous direct numerical simulation (DNS).[24] However, the change in X_{peak} with N is not straightforward. A possible explanation is as follows: X_{peak} approaches the origin with an increasing number of iterations up to $N = 3$ because the vortex shedding of the largest grid bar is strengthened owing to the increase in σ. Vortex shedding from the second and third iterations may also cause X_{peak} to be smaller.[24] However, vortex shedding from the smallest grids acts to suppress vortex shedding from the largest grid bar, causing X_{peak} to be larger. The suppression of vortex shedding from the largest grid bar by the smaller grids will be discussed later. This effect can be clearly seen for CRGs in Fig. 5(d), where X_{peak} moves significantly downstream owing to the suppression of vortex shedding from the largest grid bar.

Comparing FG4 and RGs (Fig. 5(b)), FG4 generates the smallest u'_c in the downstream region (when plotted against X/X_*). Note that σ is identical for all the grids. The location of X_{peak} is around $X/X_* \sim 0.5$ for all the grids: the concept of wake interaction[3] also applies to regular grids.[4] The profiles in the decay region are much better collapsed when X is normalized by M or L_0, as shown in Fig. 5(c).

The profiles of u'_c for CRG12 and CRG15 (Fig. 5(d)) show a rapid increase near the grid, and their increase rates become smaller at around $X/X_* = 0.2$. This is clearly due to two different wake interactions: the wake interaction of the smaller grid first appears and the effect of the wake interaction of the larger grid becomes dominant after $X/X_* > 0.2$. As mentioned above, X_{peak} for CRGs is larger than that for FG4 owing to the suppression of vortex shedding from the largest grid bar. The profiles in the far downstream region are

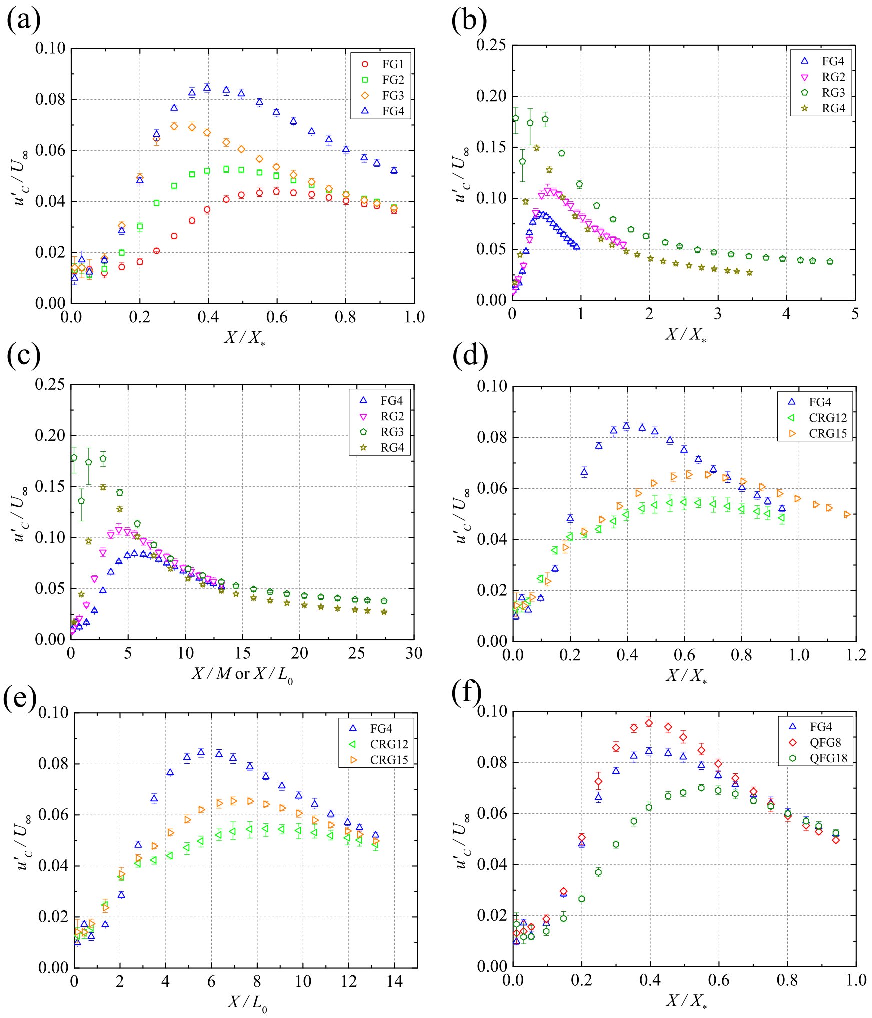

FIG. 5. Downstream profiles of the rms velocity at $Re_0 = 5900$. (a) FGs, (b) FG4 and RGs (as a function of X/X_*), (c) FG4 and RGs (as a function of X/M or X/L_0), (d) FG4 and CRGs (as a function of X/X_*), (e) FG4 and CRGs (as a function of X/L_0), and (f) FG4 and QFGs.

much better collapsed when X is normalized by L_0, as shown in Fig. 5(e), in agreement with the case for RGs. u'_c in the far downstream region has a similar magnitude to those for FG4.

The profiles of u'_c for QFG8 and QFG18 (Fig. 5(f)) show a similar trend as that for FG4. In particular, the profile of QFG8 is close to that of FG4.

It should be noted here that the anisotropy u'/v' (v': transverse rms velocity) for the fractal square grid (FG4) and the single square grid (FG1) have been extensively discussed in previous studies.[1,4,8,10,11,13,18,24] In general, the values of u'/v' for FG4 and FG1 range u'/v' = 1.1-1.3 in the decay region, and these values are similar to those measured in regular grid turbulence.[13,18,34] The two-point large-scale anisotropy has also been measured. For the fractal square grid, Discetti *et al.*[11] conducted particle image velocimetry (PIV) measurement and calculated the longitudinal and transverse correlation functions (as a function of the separation r), f and g, respectively, and compared g with the isotropic value. Their results show that large-scale (larger than λ) anisotropy persists over the examined range, whereas small-scales (smaller than λ) are approximately isotropic. For the regular grid, Valente and Vassilicos[13] measured two-point large-scale anisotropy using two hot-wire probes. For their RG60 grid with smaller M, the turbulence was almost isotropic for $r < 2M$. On the other hand, for their RG115 grid with larger M, a larger departure from isotropy was observed. Moreover, both Discetti *et al.*[11] and Valente and Vassilicos[13] found that the large-scale eddies were elongated in the streamwise direction.

B. Taylor microscale

Figure 6 shows the centerline Taylor microscale λ normalized by L_0. Here, λ is calculated by

$$\lambda^2 = \frac{u'^2_c}{\langle(\partial u_c/\partial x)^2\rangle} = \frac{\displaystyle\int_{k_{min}}^{k_{max}} E_{11}(k_1)dk_1}{\displaystyle\int_{k_{min}}^{k_{max}} k_1^2 E_{11}(k_1)dk_1}, \tag{3}$$

where $k_{min} = 2\pi f_{min}/U_c$ (U_c is the centerline mean velocity) is the lowest wavenumber which is determined from the data number and the sampling rate, and $k_{max} = 2\pi f_{max}/U_c$ is the cutoff wavenumber.[34] Here, f_{min} and f_{max} are the lowest and cutoff frequencies, respectively.

For FGs (Fig. 6(a)), FG1, FG2, and FG3 show monotonic increases in λ at $0.3 < X/X_* < 0.8$ whereas λ for FG4 is almost constant in this region, in agreement with previous studies.[1–4]

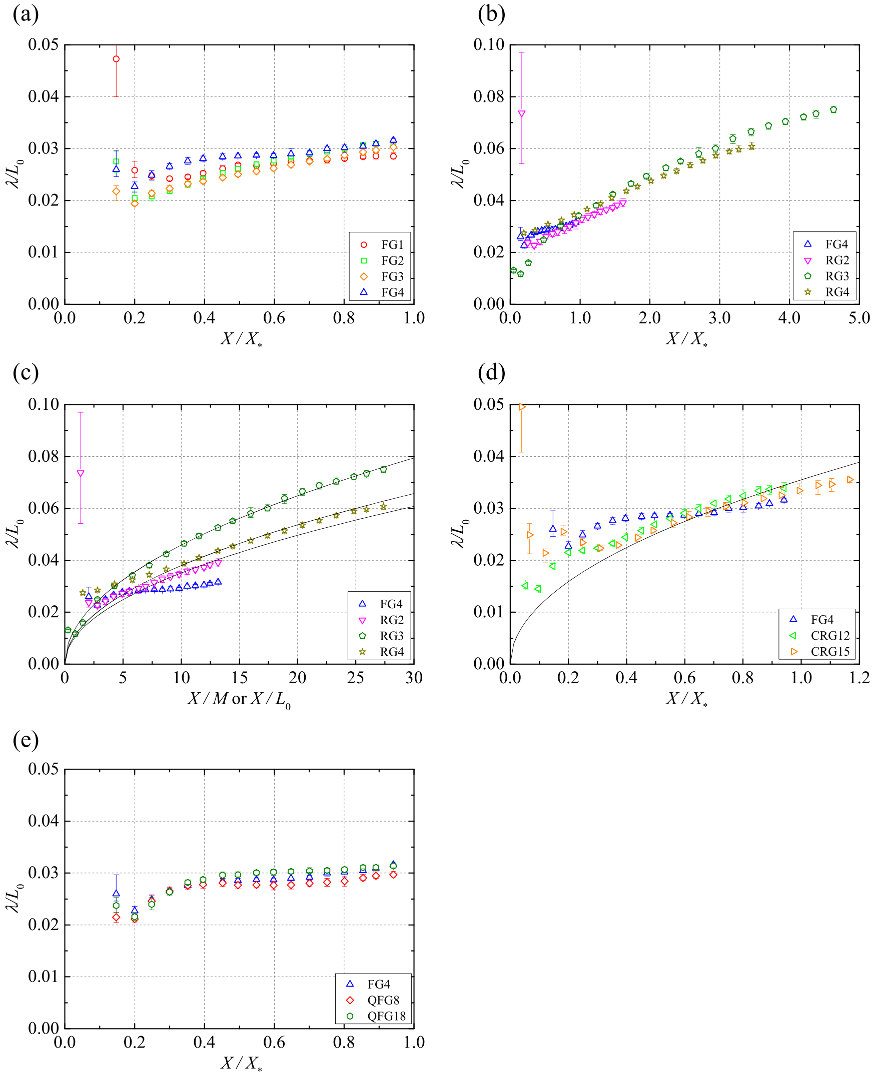

FIG. 6. Downstream profiles of the Taylor microscale at Re_0 = 5900. (a) FGs, (b) FG4 and RGs (as a function of X/X_*), (c) FG4 and RGs (as a function of X/M or X/L_0), (d) FG4 and CRGs, and (e) FG4 and QFGs.

Thus, the smallest grid element of FG4 plays an important role for constant λ in the decay region.

The profiles of λ for RGs (Fig. 6(b)) show monotonic increases in the downstream direction. The profiles of λ appear more collapsed when plotted against X/X_* rather than X/M or X/L_0 (Fig. 6(c)). Here, $\lambda \propto X^{0.5}$,[4,14,34] assuming that the virtual origins X_0 are zero,[4] are drawn in Fig. 6(c) for reference. The profiles for RGs in the decay region are well-fitted by $\lambda \propto X^{0.5}$, whereas that for FG4 is not.

The profiles of λ for CRGs (Fig. 6(d)) show monotonic increases at $0.3 < X/X_*$ as for RGs. Owing to the smaller grids of CRGs, profiles of λ for CRGs in the near-grid region are different from those of RGs. The profiles are also different from that of FG4. Thus, a simple combination of large and small grids does not generate turbulence with constant λ. In the downstream region of $0.4 < X/X_*$, the profiles for CRGs are well-fitted by $\lambda \propto X^{0.5}$ (solid line).

On the other hand, the profiles of λ for QFGs (Fig. 6(e)) show good agreement with that of FG4. A comparison of λ for CRGs and QFGs suggests that the spatial arrangement of smaller grids (i.e., the existence of "shielding" and "open" areas) is an important factor in reproducing the turbulence generated by FG4.

C. Integral length scale

Figure 7 shows the centerline integral length scale L_u normalized by L_0. Here, L_u is calculated by the integration of the auto-correlation coefficient over the time lag from zero to the first zero-crossing point.

For FG (Fig. 7(a)), the effect of iteration number N on L_u is similar to that on λ. Thus, it is suggested that the smallest grid element of FG4 plays an important role for constant L_u as well as constant λ in the decay region.

The profiles of L_u for RG3 and RG4 (Fig. 7(b)) show monotonic increases in the downstream direction. L_u for RG2 increases slightly in the downstream direction, but its rate is clearly smaller than those for RG3 and RG4. Here, $L_u \propto X^{0.4}$, assuming Saffman turbulence[34,40] and zero virtual origins ($X_0 = 0$), is drawn in Fig. 7(c) for reference. The profiles for RG3 and RG4 in the decay region are well-fitted by $L_u \propto X^{0.4}$, whereas those for FG4 and RG2 are not: the profile for RG2 is close to that of FG4. Note that the profile of λ for RG2 is different from that of FG4. The result suggests that the development (or slope) of L_u is not solely determined by M. One of the possible causes affecting the streamwise development of L_u is homogeneity/inhomogeneity (i.e., the relative size of L_u

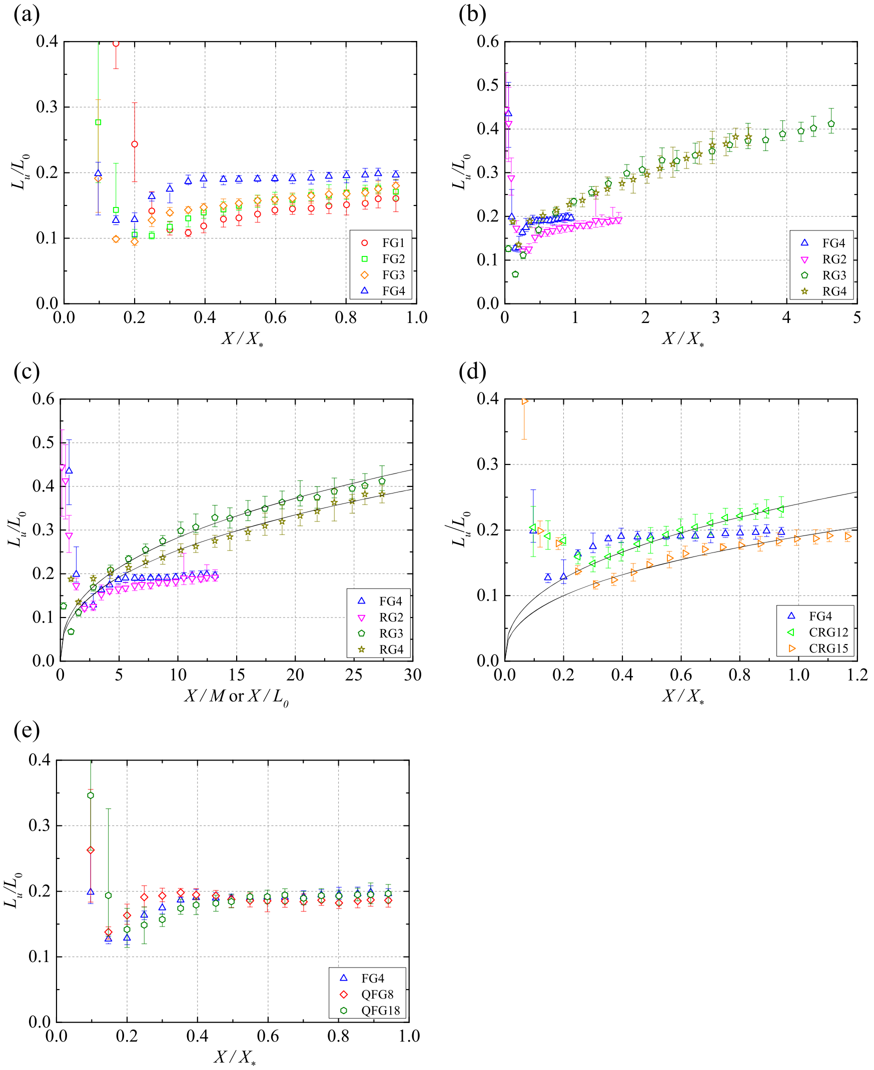

FIG. 7. Downstream profiles of the integral length scale at $Re_0 = 5900$. (a) FGs, (b) FG4 and RGs (as a function of X/X_*), (c) FG4 and RGs (as a function of X/M or X/L_0), (d) FG4 and CRGs, and (e) FG4 and QFGs.

compared with the test section's width). For RG3 and RG4, L_u at $x/M = 5$ is about 1/20 of the test section's width, whereas that for RG2 is only about 1/10. Note that in the far-downstream region (typically $X > 50M$), Kitamura *et al.*[34] showed that $L_u \propto (X - X_0)^{0.4}$ for all grids with different M (10 mm, 20 mm, and 25 mm with cylinder or square bars). In their experiments, L_u at the most downstream location is less than 1/20 of the test section's height (and less than 1/50 of the test section's width).

The profiles of L_u for CRGs (Fig. 7(d)) show monotonic increases at $0.3 < X/X_*$ as for RGs. Like λ, owing to the smaller grids of CRGs, profiles of L_u for CRGs in the near-grid region are different from those of RGs. The profiles are also different from that of FG4. Thus, like λ, a simple combination of large and small grids does not generate turbulence with constant L_u.

On the other hand, the profiles of L_u for QFGs (Fig. 7(e)) show good agreement with that for FG4.

D. Turbulent Reynolds numbers

Figure 8 shows the centerline turbulent Reynolds number Re_λ. The effects of the iteration number N on Re_λ (Fig. 8(a)) are similar to those on u'_c (Fig. 5(a)) because the effects of N on λ (Fig. 6(a)) are not very significant and the streamwise variation of λ is small.

The profiles of Re_λ for FG4 and RGs (Figs. 8(b) and 8(c)) appear more collapsed when plotted against X/X_* rather than X/M or X/L_0. Thus, it is suggested that wake interaction is a key phenomenon determining the profile of Re_λ rather than mesh size M or L_0 for a given Re_0. Figure 8(c) shows that FG4 produces the largest Re_λ in most decay regions when plotted against X/M or X/L_0. In particular, a comparison between FG4 and RG2 is interesting because both have the same mesh size (M or L_0) and the same σ. The different Re_M for FG4 and RG2 is a possible reason: $Re_M = 82\,600$ for FG4 (L_0 is used for the mesh size) and $Re_M = 48\,100$ for RG2. Thus, we also plotted Re_λ for RG2 at $Re_M = 82\,600$: the profile is similar to that of FG4. Another important feature in Re_λ for FG4 is its rapid decay.[1,3,4,8,10,24,30] This tendency was also confirmed for RG2 at the same Re_M.

The magnitudes of Re_λ for CRGs (Fig. 8(d)) are comparable to that of FG4 in the far-downstream region. As confirmed previously, the effects of two different wake interaction lengths due to the large and small grids are also confirmed here.

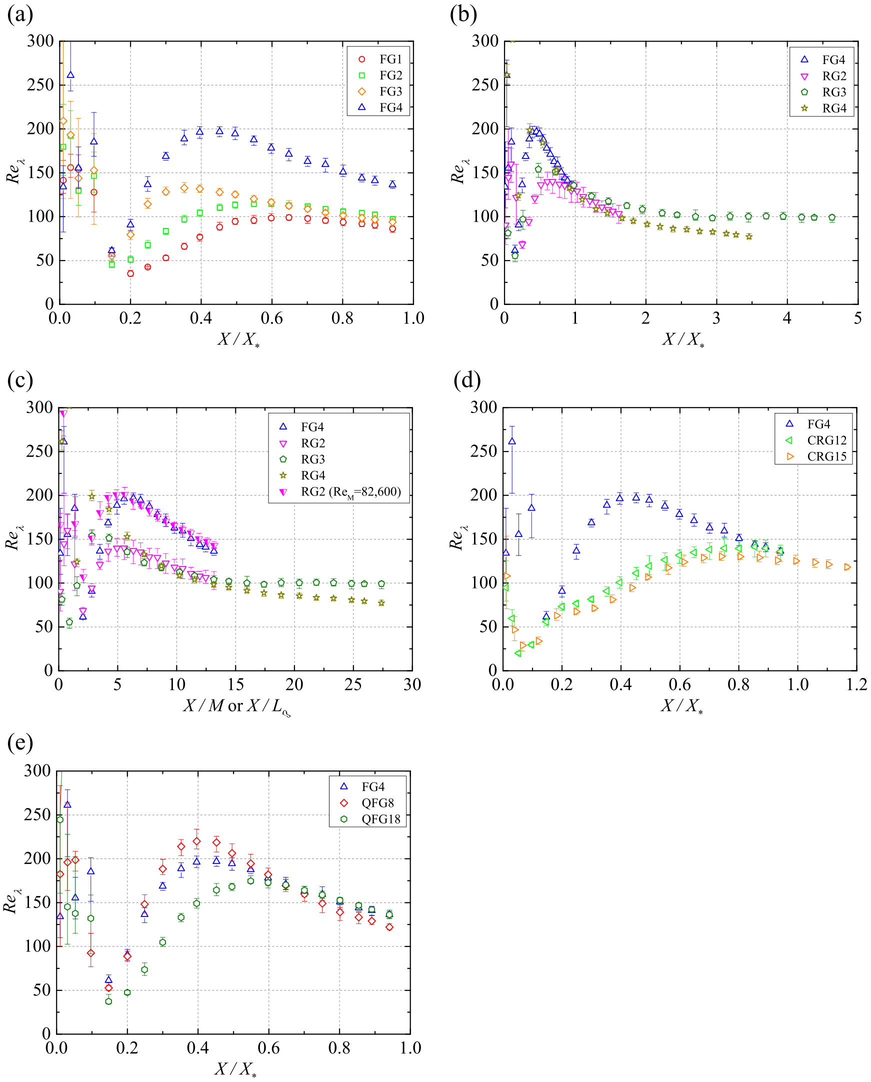

FIG. 8. Downstream profiles of the turbulent Reynolds number at $Re_0 = 5900$. (a) FGs, (b) FG4 and RGs (as a function of X/X_*), (c) FG4 and RGs (as a function of X/M or X/L_0), (d) FG4 and CRGs, and (e) FG4 and QFGs. For RG2, the result for $Re_M = 82\,600$ (same Re_M as FG4 at $Re_0 = 5900$) is also plotted in Fig. 8(c).

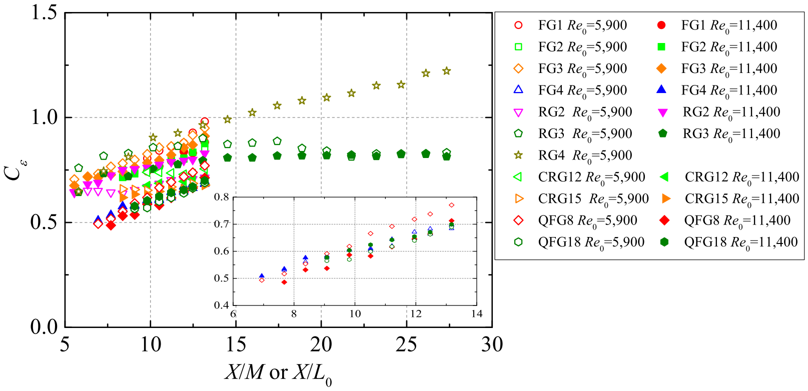

FIG. 9. Dissipation coefficient vs. X/M or X/L_0.

The profiles also suggest that a simple combination of large and small grids does not reproduce similar turbulence as that generated by FG4, as already confirmed by the profiles of λ and L_u. It is worth noting that CRG12 has the same L_0 and t_0 (and therefore the same Re_0 and Re_M) as those of FG4. In addition, both have the smaller grids. Nevertheless, FG4 produces much larger Re_λ in the near-grid field compared with CRG12.

Figure 8(e) shows that the profiles of Re_λ for QFG8 show better agreement with that of FG4 compared with QFG18. Recall that L_r for QFG8 is close to that for FG4. Thus, for QFGs, it is suggested that L_r is more important than t_r to reproduce a similar Re_λ for FG4 (for a given Re_0). Note that FG4, CRG12, QFG8, and QFG18 have the same L_0 and t_0 (and therefore the same Re_0 and Re_M). Among all the grids, RG2 at $Re_M = 82\,600$ and QFG8 ($Re_M = 82\,600$) produce similar profiles for Re_λ as that of FG4. However, note that the profile of λ for RG2 is different from that of FG4. For QFG8, all turbulence characteristics shown herein show similar profiles to those for FG4.

E. Dissipation and non-equilibrium nature

In this subsection, dissipation and non-equilibrium characteristics in the TKE decay region are investigated.

Figure 9 shows the TKE dissipation coefficient C_ε plotted against X/M or X/L_0. As already found in previous studies,[6,14] C_ε increases near the grid and becomes nearly constant in the far-downstream region. Note that a constant C_ε region was not observed for FGs and QFGs because of limited test section length. Thus, there is a possibility that the non-equilibrium regions are wider for FGs and QFGs. Note that, for RG2, RG3, CRG12, and CRG15, C_ε is almost constant, i.e., within the equilibrium range, at the downstream location. The profiles near the grid show the dependency on grid geometries. Note that the continuous increase for RG4 in the far-downstream region may be due to the low-Reynolds-number effect, as will be confirmed in Fig. 10: Re_λ in this region is too small to attain a constant C_ε.[31,32] An important comparison may be made between FG4 and QFG (see the inset of Fig. 9), as their profiles are quite similar.

Figure 10 shows the C_ε plotted against Re_λ in a log-log plot. The lines show $C_\varepsilon \propto Re_\lambda^{-1}$. For FG4 and QFGs, $C_\varepsilon \propto Re_\lambda^{-1}$, as found in previous studies[2,4,6,30] (see the inset of Fig. 10). For other grids, C_ε also decreases as Re_λ increases, although the slopes are somewhat smaller in magnitude than -1. Note again that, for RG4, there may be a low-Reynolds-number effect: as shown in much of the literature, C_ε decreases as Re_λ increases at low Reynolds numbers (typically $Re_\lambda < 50$–100 [30–34]). An important finding here is that, for all grids, the profiles are roughly collapsed for each Re_0: Re_0 is a key parameter for C_ε profiles. We therefore used Re_0 instead of Re_M as a global/inlet Reynolds number in Eq. (2). Figures 11(a) and 11(b) compare C_ε plotted against $Re_M^{1/2}/Re_\lambda$ and $Re_0^{1/2}/Re_\lambda$. Figure 11(a) shows that profiles for the regular grids (RG2, RG3, and RG4) and for multi-scale grids are somewhat different. On the other hand, C_ε is better collapsed when plotted against $Re_0^{1/2}/Re_\lambda$. This suggests that Re_0 is a more appropriate choice as a global/inlet Reynolds number than Re_M.

Next, we investigate the dependency of C_ε on Re_L for each grid. Figure 12 shows C_ε plotted against Re_L in a log-log plot. For FGs (Fig. 12(a)), C_ε becomes more inversely proportional to Re_L as the iteration number N increases. For RGs, the relation $C_\varepsilon \propto Re_L^{-1}$ is not clearly observed for RG2 and RG3 at $Re_0 = 5900$. C_ε for RG4 appears to be inversely proportional to Re_L, but the low-Reynolds-number effect should be taken into account for this case. For CRGs (Fig. 12(c)), C_ε scarcely shows the relation $C_\varepsilon \propto Re_L^{-1}$. On the other hand, C_ε profiles for QFGs are similar to RG4 and show a clear relationship: $C_\varepsilon \propto Re_L^{-1}$.

Figure 13 shows the relationship between L_u/λ and Re_λ. As shown in Fig. 13(a), a wide non-equilibrium region is observed for FG3 and FG4 of the fractal square grid. Despite the limited test section length, the result is expected to remain unchanged for the following reason: Re_λ is still rapidly decreasing for FG4 (Fig. 8(a) for $Re_0 = 5900$: profiles

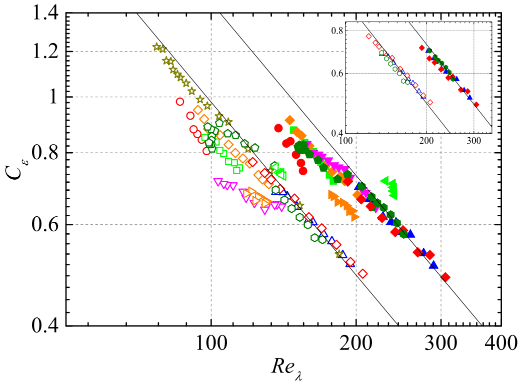

FIG. 10. Dissipation coefficient vs. Re_λ. Symbols as in Fig. 9.

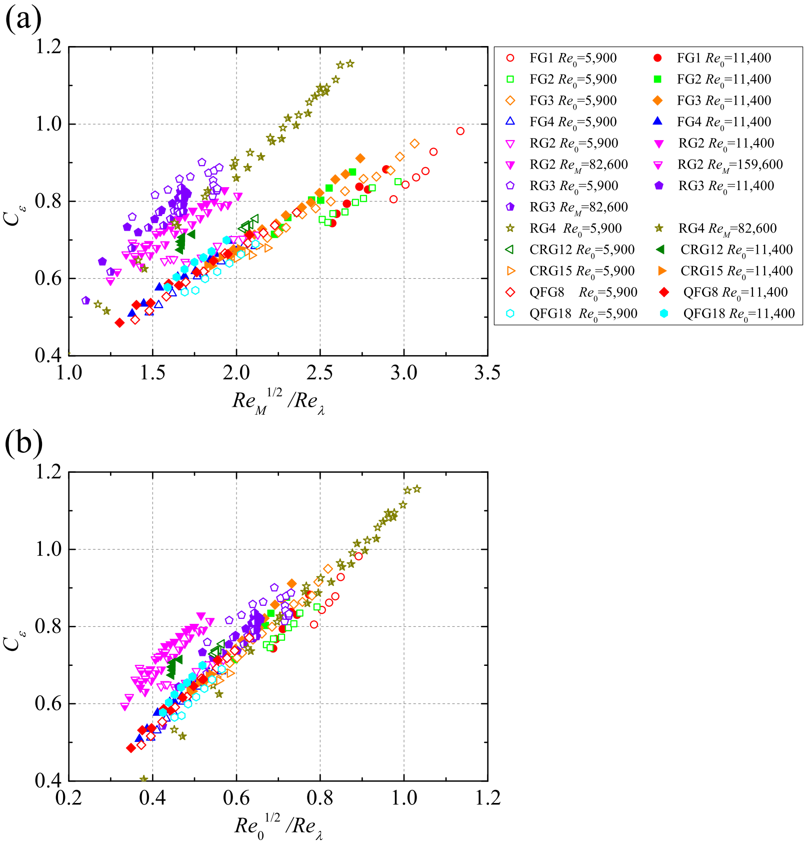

FIG. 11. Dissipation coefficient vs. (a) $Re_M^{1/2}/Re_\lambda$ and (b) $Re_0^{1/2}/Re_\lambda$.

are qualitatively similar for $Re_0 = 11\,400$, which are not shown here), whereas the changes in Re_λ are smaller for FG1 ∼ 3. The same tendency has been confirmed for FG1 and FG4 in our previous DNS.[24] Note that the change in Re_λ becomes smaller in the far downstream region of grid turbulence (e.g., for Saffman turbulence, which is close to regular grid turbulence, $Re_\lambda \propto X^{-0.1}$).[34] This suggests that the constant L_u/λ region is wider to the small Re_λ side for FG4 whereas that region may not be largely extended to the small Re_λ side for FG1 ∼ 3. Recall that Re_λ decreases in the downstream region. The clear relation $C_\varepsilon \propto Re_L^{-1}$ seen only for FG3 and FG4 (Fig. 12(a)) also supports a distinct non-equilibrium region for

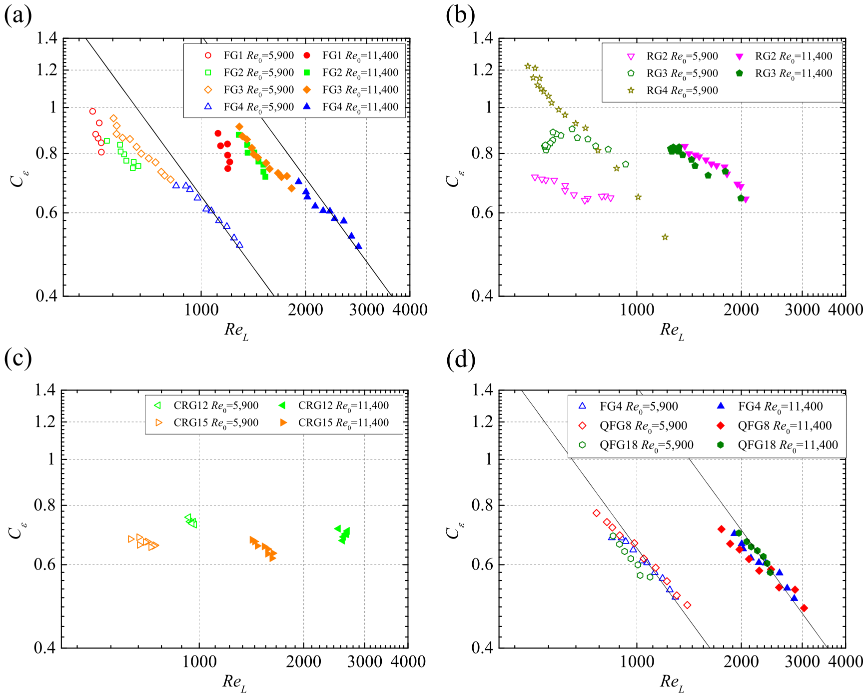

FIG. 12. Dissipation coefficient vs. Re_L. (a) FGs, (b) RGs, (c) CRGs, and (d) FG4 and QFGs.

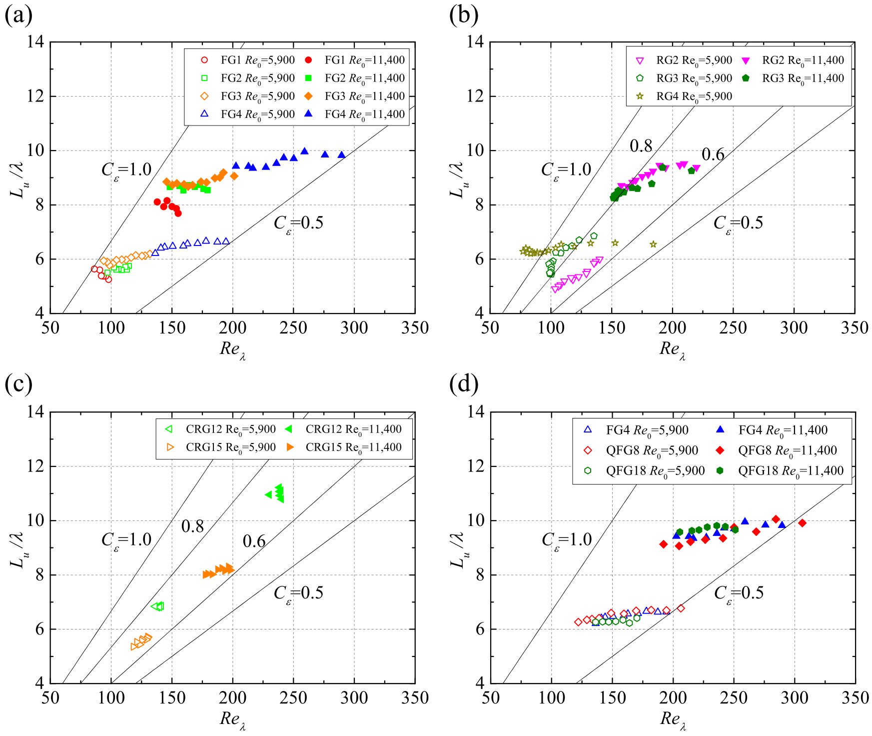

FIG. 13. L_u/λ vs. Re_λ. (a) FGs, (b) RGs, (c) CRGs, and (d) FG4 and QFGs.

FG3 and FG4. For RGs (Fig. 13(b)), RG2 at $Re_0 = 5900$ has a relatively wide equilibrium region in which $L_u/\lambda \propto Re_\lambda$. For RG2 and RG3 at $Re_0 = 11\,400$, the near-grid region (large Re_λ) shows a non-equilibrium nature (i.e., nearly constant L_u/λ) and attains equilibrium in the far-downstream region (small Re_λ). The result is consistent with a previous study:[6] however, the non-equilibrium range is not very wide compared with that for FG4. CRGs (Fig. 13(c)) scarcely show non-equilibrium nature. Again, together with the profile of C_ε in Fig. 12(c), it is found that a simple combination of large and small grids does not reproduce a wide non-equilibrium region like that resulting from the use of the fractal square grid (FG4). On the other hand, QFGs (Fig. 13(d)) show almost the same profile as for FG4. This suggests that the combination of a large square grid and inhomogeneously arranged smaller grids (i.e., the existence of "shielding" and "open" areas) produces an elongated non-equilibrium region.

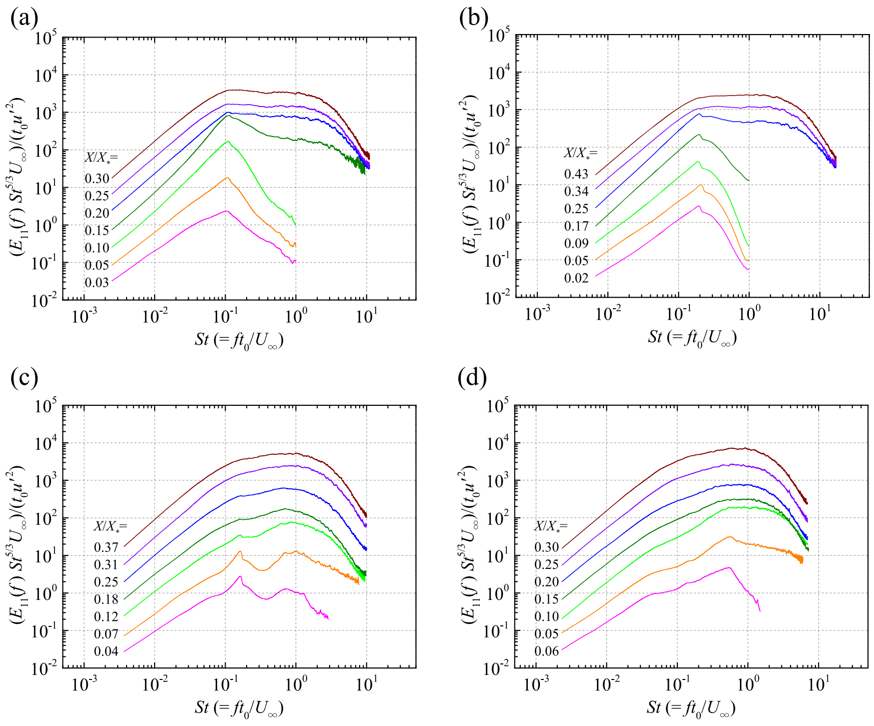

FIG. 14. Downstream variations in one-dimensional power spectra ($Re_0 = 5900$). (a) FG4, (b) RG2, (c) CRG15, and (d) CRG12.

F. Effects of multi-scale energy input

Before closing the paper, effects of multi-scale energy input are briefly discussed. Figure 14 shows the downstream variations in one-dimensional power spectra for $Re_0 = 5900$. The frequency f is normalized using t_0 and U_∞ (i.e., the Strouhal number for the largest grid bar), and the spectra are multiplied by $f^{5/3}$ ($=St^{5/3}$).[17] The spectra at each downstream location are shifted vertically for clearer investigation. The spectra for FG4 has a single peak near $St \sim 0.1$ in the upstream region of $X/X_* < 0.15$. This result is consistent with previous studies.[16,17] The spectra for QFGs are similar to those for FG4, and thus they are omitted here. The spectra for CRG15 clearly show the two distinct peaks associated with vortex shedding from large and small grids. For CRG12, the vortex shedding from the small grids prevails and no clear peak associated with vortex shedding from the large grid is apparent. The most interesting consequence is that, for CRGs, vortex shedding of the smaller grids strongly suppresses the vortex shedding of the largest grid bar, whereas for FG4 and QFG8, vortex shedding of the smaller grids does not strongly suppress the vortex shedding of the largest grid bar. The spectra for FG4 (and QFG8, which are not shown here) are similar to those for RG2. This leads to the possible conclusion that when the vortex shedding of the largest grid bar is strongly suppressed by the vortex shedding of the smaller grids, non-equilibrium behavior may be suppressed. Note that C_ε is nearly constant in the decay region for CRGs (see Fig. 12(c)).

IV. CONCLUSIONS

A total of 11 grids in four families, including single- and multi-scale grids, were tested to investigate the development and decay characteristics of grid-generated turbulence. Special attention has been focused on dissipation and the non-equilibrium nature in the decay region.

The main results are as follows.

1. A wide non-equilibrium region is observed for FG3 and FG4 (with three and four iterations) of the fractal square grid. The smallest grid elements of the fractal square grid play an important role in generating a nearly constant Taylor microscale λ and integral length scale L_u in the decay region.
2. X_{peak} is determined mainly by X_* as already shown in previous studies. The profiles of u'_c in the far downstream region are better collapsed when the streamwise distance is normalized by M or L_0.
3. A simple combination of large and small grids does not reproduce elongated non-equilibrium regions as observed for fractal square grids. Instead, a combination of a large square grid and inhomogeneously arranged smaller grids (i.e., the existence of "shielding" and "open" areas) produces elongated non-equilibrium regions.
4. Re_0 is a more appropriate choice as a global/inlet Reynolds number than Re_M, i.e., $C_\varepsilon \propto Re_0^{1/2}/Re_\lambda$ (equivalently, $C_\varepsilon \propto Re_0/Re_L$) rather than $C_\varepsilon \propto Re_M^{1/2}/Re_\lambda$ (equivalently $C_\varepsilon \propto Re_M/Re_L$).

Regarding our conclusion 3, comparison between FG4 (as well as QFGs) and CRGs indeed suggests that inhomogeneity of grid geometry causes non-equilibrium behavior. However, although "inhomogeneous" grids yield wider spatial ranges of non-equilibrium dissipation as shown in this paper, this behavior does not necessarily occur as a result of the one-point inhomogeneity that the grids may or may not impose on the turbulent flow. In the turbulent flows produced by regular and fractal grids, spatial turbulence inhomogeneities in the one-point statistics do exist and cause turbulence production and transport in the one-point energy equation.[10,13] However, these inhomogeneities do not affect the two-point energy equation on the scales for which the inertial energy cascade occurs.[39] This would suggest that the cascade mechanism of the turbulence dissipation is not affected by one-point inhomogeneities. In other words, the inhomogeneity of a two-point energy balance at the right length-scales is important, rather than the inhomogeneity of the one-point energy balance. In fact, DNS studies of Goto and Vassilicos[41,42] showed that non-equilibrium dissipation scaling is also present even though the interscale energy dynamics are determined by the Lin equation, which is not affected by single-point inhomogeneities.

Our new grid type, i.e., quasi-fractal grids (QFGs), is easier to fabricate compared to the well-established fractal square grids while generating similar turbulent fields. This feature is helpful in possible practical applications of fractal grids.[25–29]

ACKNOWLEDGMENTS

The authors acknowledge the valuable comments of Professor J. C. Vassilicos (Imperial College London), Professor S. Goto (Osaka University), Dr. T. Watanabe (Nagoya University), Dr. T. Kitamura (Nagoya University), and three anonymous referees. The authors would like to thank Mr. S. Nakamura (Graduate School of Nagoya University) for his kind help to this study. This work was supported by JSPS KAKENHI Grant No. 25289030.

[1] D. Hurst and J. C. Vassilicos, "Scalings and decay of fractal-generated turbulence," Phys. Fluids **19**, 035103 (2007).

[2] R. E. Seoud and J. C. Vassilicos, "Dissipation and decay of fractal-generated turbulence," Phys. Fluids **19**, 105108 (2007).

[3] N. Mazellier and J. C. Vassilicos, "Turbulence without Richardson-Kolmogorov cascade," Phys. Fluids **22**, 075101 (2010).

[4] P. C. Valente and J. C. Vassilicos, "The decay of turbulence generated by a class of multiscale grids," J. Fluid Mech. **687**, 300 (2011).

[5] P.-Å. Krogstad and P. A. Davidson, "Freely decaying, homogeneous turbulence generated by multi-scale grids," J. Fluid Mech. **680**, 417 (2011).

[6] P. C. Valente and J. C. Vassilicos, "Universal dissipation scaling for nonequilibrium turbulence," Phys. Rev. Lett. **108**, 214503 (2012).

[7] P. C. Valente and J. C. Vassilicos, "Dependence of decaying homogeneous isotropic turbulence on inflow conditions," Phys. Lett. A **376**, 510 (2012).

[8] R. Gomes-Fernandes, B. Ganapathisubramani, and J. C. Vassilicos, "Particle image velocimetry study of fractal-generated turbulence," J. Fluid Mech. **711**, 306 (2012).

[9] P.-Å. Krogstad and P. A. Davidson, "Near-field investigation of turbulence produced by multi-scale grids," Phys. Fluids **24**, 035103 (2012).

[10] K. Nagata, Y. Sakai, T. Inaba, H. Suzuki, O. Terashima, and H. Suzuki, "Turbulence structure and turbulence kinetic energy transport in multiscale/fractal-generagted turbulence," Phys. Fluids **25**, 065102 (2013).

[11] S. Discetti, I. B. Ziskin, T. Astarita, R. J. Adrian, and K. P. Prestridge, "PIV measurements of anisotropy and inhomogeneity in decaying fractal generated turbulence," Fluid Dyn. Res. **45**, 061401 (2013).

[12] R. J. Hearst and P. Lavoie, "Scale-by-scale energy budget in fractal element grid-generated turbulence," J. Turbul. **15**, 540 (2014).

[13] P. C. Valente and J. C. Vassilicos, "The non-equilibrium region of grid-generated decaying turbulence," J. Fluid Mech. **744**, 5 (2014).

[14] R. J. Hearst and P. Lavoie, "Decay of turbulence generated by a square-fractal-element grid," J. Fluid Mech. **741**, 567 (2014).

[15] R. J. Hearst and P. Lavoie, "Velocity derivative skewness in fractal-generated, non-equilibrium grid turbulence," Phys. Fluids **27**, 071701 (2015).

[16] R. Gomes-Fernandes, B. Ganapathisubramani, and J. C. Vassilicos, "The energy cascade in near-field non-homogeneous non-isotropic turbulence," J. Fluid Mech. **771**, 676 (2015).

[17] S. Laizet, J. Nedić, and J. C. Vassilicos, "The spatial origin of −5/3 spectra in grid-generated turbulence," Phys. Fluids **27**, 065115 (2015).

[18] K. Nagata, H. Suzuki, Y. Sakai, T. Hayase, and T. Kubo, "Direct numerical simulation of turbulence characteristics generated by fractal grids," Int. Rev. Phys. **2**(6), 400 (2008).

[19] S. Laizet and J. C. Vassilicos, "Multiscale generation of turbulence," J. Multiscale Modell. **1**, 177 (2009).

[20] H. Suzuki, K. Nagata, Y. Sakai, and T. Hayase, "Direct numerical simulation of turbulent mixing in regular and fractal grid turbulence," Phys. Scr. **T142**, 014065 (2010).

[21] S. Laizet, E. Lamballais, and J. C. Vassilicos, "A numerical strategy to combine high-order schemes, complex geometry and parallel computing for high resolution DNS of fractal generated turbulence," Comput. Fluids **39**, 471 (2010).

[22] S. Laizet and J. C. Vassilicos, "DNS of fractal-generated turbulence," Flow, Turbul. Combust. **87**, 673 (2011).

[23] S. Laizet, J. C. Vassilicos, and C. Cambon, "Interscale energy transfer in decaying turbulence and vorticity–strain-rate dynamics in grid-generated turbulence," Fluid Dyn. Res. **45**, 061408 (2013).

[24] Y. Zhou, K. Nagata, Y. Sakai, H. Suzuki, Y. Ito, O. Terashima, and T. Hayase, "Relevance of turbulence behind the single square grid to turbulence generated by regular- and multiscale-grids," Phys. Fluids **26**, 075105 (2014).

[25] F. C. G. A. Nicolleau, S. M. M. Salim, and A. F. Nowakowski, "Experimental study of a turbulent pipe flow through a fractal plate," J. Turbul. **12**, N44 (2011).

[26] B. Manshoor, F. C. G. A. Nicolleau, and S. B. M. Beck, "The fractal flow conditioner for orifice plate flow meters," Flow Meas. Instrum. **22**, 208 (2011).

[27] J. Nedic, B. Ganapathisubramani, J. C. Vassilicos, J. Borée, L. Brizzi, and A. Spohn, "Aeroacoustic performance of fractal spoilers," AIAA J. **50**, 2695 (2012).

[28] A. A. Verbeek, T. W. F. M. Bouten, G. G. M. Stoffels, B. J. Georts, and T. H. van der Meer, "Fractal turbulence enhancing low-swirl combustion," Combust. Flame **162**, 129 (2015).

[29] T. Sponfeldner, N. Soulopoulos, F. Beyrau, Y. Hardalupas, A. M. K. P. Taylor, and J. C. Vassilicos, "The structure of turbulent flames in fractal- and regular-grid-generated turbulence," Combust. Flame **162**, 3379 (2015).

[30] J. C. Vassilicos, "Dissipation in turbulent flows," Annu. Rev. Fluid Mech. **47**, 95 (2015).

[31] K. R. Sreenivasan, "On the scaling of the turbulence energy dissipation rate," Phys. Fluids **27**, 1048 (1984).

[32] K. R. Sreenivasan, "An update on the energy dissipation rate in isotropic turbulence," Phys. Fluids **10**, 528 (1998).

[33] W. J. T. Bos, L. Shao, and J.-P. Bertoglio, "Spectral imbalance and the normalized dissipation rate of turbulence," Phys. Fluids **19**, 045101 (2007).

[34] T. Kitamura, K. Nagata, Y. Sakai, A. Sasoh, O. Terashima, H. Saito, and T. Harasaki, "On invariants in grid turbulence at moderate Reynolds numbers," J. Fluid Mech. **738**, 378 (2014).

[35] A. Tsinober, *An Informal Conceptual Introduction to Turbulence* (Springer, 2009).

[36] C. H. Gibson, "The first turbulence and first fossil turbulence," Flow, Turbul. Combust. **72**, 161 (2004).

[37] C. H. Gibson, "Turbulence and turbulent mixing in natural fluids," Phys. Scr. **T142**, 014030 (2010).

[38] J. C. Isaza, R. Salazar, and Z. Warhaft, "On grid-generated turbulence in the near- and far field regions," J. Fluid Mech. **753**, 402 (2015).

[39] P. C. Valente and J. C. Vassilicos, "The energy cascade in grid-generated non-equilibrium decaying turbulence," Phys. Fluids **27**, 045103 (2015).

[40] P.-Å. Krogstad and P. A. Davidson, "Is grid turbulence Saffman turbulence?," J. Fluid Mech. **642**, 373 (2010).

[41] S. Goto and J. C. Vassilicos, "Energy dissipation and flux laws for unsteady turbulence," Phys. Lett. A **379**, 1144 (2015).

[42] S. Goto and J. C. Vassilicos, "Local equilibrium hypothesis and Taylor's dissipation law," Fluid Dyn. Res. **48**, 021402 (2016).